Downloaded from orbit.dtu.dk on: Mar 20, 2023

DTU Library

Acousto-optical phonon excitation in cubic piezoelectric slabs and crystal growth orientation effects

Willatzen, Morten; Duggen, Lars

Published in:
Physical Review B

Link to article, DOI:
10.1103/PhysRevB.95.035310

Publication date:
2017

Document Version
Publisher's PDF, also known as Version of record

Link back to DTU Orbit

Citation (APA):
Willatzen, M., & Duggen, L. (2017). Acousto-optical phonon excitation in cubic piezoelectric slabs and crystal growth orientation effects. *Physical Review B*, *95*(3), [035310]. https://doi.org/10.1103/PhysRevB.95.035310

General rights
Copyright and moral rights for the publications made accessible in the public portal are retained by the authors and/or other copyright owners and it is a condition of accessing publications that users recognise and abide by the legal requirements associated with these rights.

- Users may download and print one copy of any publication from the public portal for the purpose of private study or research.
- You may not further distribute the material or use it for any profit-making activity or commercial gain
- You may freely distribute the URL identifying the publication in the public portal

If you believe that this document breaches copyright please contact us providing details, and we will remove access to the work immediately and investigate your claim.

Acousto-optical phonon excitation in cubic piezoelectric slabs and crystal growth orientation effects

Lars Duggen*
University of Southern Denmark, Mads Clausen Institute, Sønderborg 6400, Denmark

Morten Willatzen
Technical University of Denmark, Department of Photonics Engineering, Kongens Lyngby 2800, Denmark
(Received 10 November 2016; revised manuscript received 31 December 2016; published 30 January 2017)

In this paper we investigate theoretically the influence of piezoelectric coupling on phonon dispersion relations. Specifically we solve dispersion relations for a fully coupled zinc-blende freestanding quantum well for different orientations of the crystal unit cell. It is shown that the phonon mode density in GaAs can change by a factor of approximately 2–3 at $q_x a = 1$ for different crystal-growth directions relative to the slab thickness direction. In particular, it is found that optical and acoustic phonon modes are always piezoelectrically coupled, independent of the crystal-growth direction, and will be jointly excited by electrical stimulus. We demonstrate this for an electrically excited freestanding slab for two cases of high-symmetry crystal-growth directions and finally show the impact of the Drude model for permittivity on the phonon dispersion. In particular, it is verified that the piezoelectric effect leads to a drastically enhanced coupling of acoustic and optical phonon modes and increase in the local phonon density of states near the plasma frequency where the permittivity approaches zero.

DOI: 10.1103/PhysRevB.95.035310

I. INTRODUCTION

Quantized lattice vibrations—phonons—are a major contributor to electron scattering mechanisms in modern quantum semiconductor structures, influencing electron transport, and thereby efficiency properties, especially at high temperatures [1]. While usually leading to a degradation of electronic performance, electron-phonon interactions can be employed to design device characteristics by appropriate geometry and well-controlled external conditions [2]. Recently, there have been several studies on the effect of phonons on excited states, utilizing phonons to achieve population inversion in InGaAs quantum dot systems [3–6]. Also, phonon-assisted gain in double quantum dot masers has been reported recently [7]. Other intriguing studies include the strong effect on dephasing mechanisms in quantum cavity systems [8–10] with implications on quantum information technology, since dephasing destroys entanglement which is essential for Quantum Information Processing purposes [11,12].

The piezoelectric effect is an inherent electromechanical coupling occurring in a number of common semiconductor materials such as GaAs, GaN, and ZnO. An example of exploiting this effect in semiconductors is the generation of gate voltages in (nano)piezotronics [13]. On the other hand, the piezoelectric effect also influences the reduced electron mobility caused by electron-phonon interaction in, e.g., two-dimensional MoS_2, which is also used in piezotronic devices [14,15]. Further, the effect is essential for single-electron transport by surface acoustic waves [16]. Surface phonons have been measured experimentally [17], leading to an advancement in both quantum phononics and plasmonics, where the surface acoustic waves are used to assist plasmon excitation by light [18,19]. For applications in quantum information processing, phonon generation in gated GaAs/AlGaAs quantum dots by virtue of the piezoelectric effect also has decisive impact on qubit state dynamics through electric manipulation of the latter [20–22].

In this paper we investigate the effect of anisotropy, piezoelectricity, and crystal orientation on the phonon dispersion in a freestanding GaAs quantum-well slab. Classically, previous treatments of phonons have typically used isotropic assumptions and have treated acoustic and optical phonons separately [23–25]. It has been shown that the exclusion of anisotropy and the piezoelectric effect leads to significant changes in the phonon dispersion curves for a piezoelectric slab, and that, due to the piezoelectric coupling, certain acoustic phonons are coupled with the electric potential and hence interact with electromagnetic waves, termed acousto-optical phonons [26]. The pronounced effect of anisotropy, however, stipulates that the phonon dispersion relation in a slab also depends on the crystal orientation, just like the electromechanical coupling in general—an effect that already has been studied for other quantum systems, such as quantum-well structures where the lattice-mismatch induced strain causes electric fields in the well region, highly influential for LED applications [27,28].

We develop a framework to solve for the phonon dispersion in cubic, piezoelectric materials for an arbitrary crystal orientation and show results for high-symmetry orientations. We find that, generally, all elastic polarizations are coupled with a piezoelectric potential, hence stating that, most generally, no purely acoustic phonons can exist. Even for symmetry orientations such as the case where the in-plane wave number is aligned to a body diagonal (i.e., [111] direction), there are no pure acoustic phonons. For certain other symmetry orientations such as [011] or [001], several polarizations can decouple from the piezoelectric potential and hence give the possibility for purely acoustic phonons. The understanding of this coupling is important for processes like Raman scattering [29].

*duggen@mci.sdu.dk

 ©2017 American Physical Society

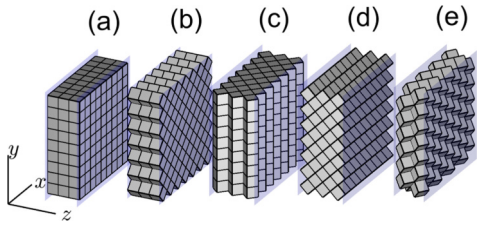

FIG. 1. Sketch of the five symmetry cases considered with $\{\theta,\phi,\psi\}$ being (a) $\{0,0,0\}$, (b) $\{0,\pi/4,0\}$, (c) $\{0,0,\pi/4\}$, (d) $\{\pi/4,0,0\}$, and (e) $\{\pi/4,0,0\}$ followed by $\{0,\cos^{-1}(1/\sqrt{3}),0\}$. The slab is defined by $-a/2 \leqslant z \leqslant a/2$ as indicated by the semitransparent planes.

II. THEORY

The equations of motion for a general piezoelectric material under the assumption of no free charge carriers are

$$\nabla \cdot \mathbf{T} = \rho \frac{\partial^2 \mathbf{u}}{\partial t^2}, \tag{1}$$

$$\nabla \cdot \mathbf{D} = 0, \tag{2}$$

with $\rho, \mathbf{T}, \mathbf{u}$, and $\mathbf{D}$ denoting mass density, stress, particle displacement, and electric displacement field, respectively.

The piezoelectric constitutive relations used in the following read

$$\mathbf{T} = \mathbf{cS} + \mathbf{e}\nabla\Phi, \tag{3}$$

$$\mathbf{D} = -\epsilon\nabla\Phi + \mathbf{eS}, \tag{4}$$

with $\mathbf{c}, \mathbf{e}, \epsilon$ being the stiffness tensor, piezoelectric stress tensor, and permittivity matrix, respectively, and $\mathbf{S}, \Phi$ are the strain and electric potential, respectively. Note that the quasistatic approximation is employed, so $\mathbf{E} = -\nabla\Phi$, $\mathbf{E}$ being the electric field. For cubic piezoelectric materials, the material parameter matrices have the form

$$\mathbf{c}_0 = \begin{bmatrix} c_{11} & c_{12} & c_{12} & 0 & 0 & 0 \\ c_{12} & c_{11} & c_{12} & 0 & 0 & 0 \\ c_{12} & c_{12} & c_{11} & 0 & 0 & 0 \\ 0 & 0 & 0 & c_{44} & 0 & 0 \\ 0 & 0 & 0 & 0 & c_{44} & 0 \\ 0 & 0 & 0 & 0 & 0 & c_{44}, \end{bmatrix}, \tag{5}$$

$$\mathbf{e}_0 = \begin{bmatrix} 0 & 0 & 0 & e_{14} & 0 & 0 \\ 0 & 0 & 0 & 0 & e_{14} & 0 \\ 0 & 0 & 0 & 0 & 0 & e_{14} \end{bmatrix}, \tag{6}$$

while ϵ is a purely diagonal matrix with the same value along the diagonal, i.e., it can be treated as a scalar. The subscript zero denotes that the material parameters are taken in the [001] direction. Due to the inherent anisotropy in cubic crystals, the parameter matrices depend on the orientation of the unit cells. The matrices given above apply to problems where the x, y, z coordinates coincide with the directions of the edges of the cube forming a unit cell. Other directions can be modeled by using rotation angles and their corresponding matrix operators

$$\mathbf{a}_x = \begin{bmatrix} 1 & 0 & 0 \\ 0 & \cos(\theta) & \sin(\theta) \\ 0 & -\sin(\theta) & \cos(\theta), \end{bmatrix}, \tag{7}$$

$$\mathbf{a}_y = \begin{bmatrix} \cos(\psi) & 0 & \sin(\psi) \\ 0 & 1 & 0 \\ -\sin(\psi) & 0 & \cos(\psi), \end{bmatrix}, \tag{8}$$

$$\mathbf{a}_z = \begin{bmatrix} \cos(\phi) & \sin(\phi) & 0 \\ -\sin(\phi) & \cos(\phi) & 0 \\ 0 & 0 & 1 \end{bmatrix}, \tag{9}$$

where $\mathbf{a}_x, \mathbf{a}_y, \mathbf{a}_z$ represent rotations of angle θ, ψ, ϕ around the x, y, and z axis, respectively.

The rotations and reference coordinate system are depicted in Fig. 1. Any orientation can be modeled by two subsequent rotations about an axis, so, e.g., a rotation that aligns the body diagonals to the xyz coordinates can be achieved by first rotating around the x axis by an angle $\theta = \pi/4$ and subsequently rotating around the new z axis by an angle $\phi = \cos^{-1}(1/\sqrt{3})$. The material parameter matrices transform accordingly as [30]

$$\mathbf{c} = \mathbf{M}\mathbf{c}_0\mathbf{M}^T, \tag{10}$$

$$\mathbf{e} = \mathbf{a}\mathbf{e}_0\mathbf{M}^T, \tag{11}$$

where $\mathbf{M}$ is a 6×6 matrix constructed by elements of $\mathbf{a}$.

For the purpose of analyzing the dispersion relation we align the coordinate system such that the in-plane wave number $q_\parallel$ is aligned with the x direction and there is no y dependence, i.e., $q_\parallel = q_x$. The slab is defined by $-a/2 \leqslant z \leqslant a/2$ as indicated by the semitransparent planes in Fig. 1 with the wave number in the z direction denoted γ. Then, searching for wave solutions in the form $\exp(i[q_x x + \gamma z])$ the four governing equations, Eqs. (1) and (2), can be written as

$$\begin{bmatrix} (c_{11}q_x^2 + 2c_{15}\gamma q_x + c_{55}\gamma^2 - \rho\omega^2) & ((c_{14}+c_{56})q_x\gamma + c_{16}q_x^2 + c_{45}\gamma^2) & ((c_{13}+c_{55})q_x\gamma + c_{15}q_x^2 + c_{35}\gamma^2) & ((e_{31}+e_{15})q_x\gamma + e_{11}q_x^2 + e_{35}\gamma^2) \\ (c_{16}q_x^2 + (c_{14}+c_{56})q_x\gamma + c_{45}\gamma^2) & (2c_{46}q_x\gamma + c_{66}q_x^2 + c_{44}\gamma^2 - \rho\omega^2) & ((c_{45}+c_{36})q_x\gamma + c_{56}q_x^2 + c_{34}\gamma^2) & ((e_{14}+e_{36})q_x\gamma + e_{16}q_x^2 + e_{34}\gamma^2) \\ (c_{15}q_x^2 + (c_{13}+c_{55})q_x\gamma + c_{35}\gamma^2) & ((c_{36}+c_{45})q_x\gamma + c_{56}q_x^2 + c_{34}\gamma^2) & (2c_{35}q_x\gamma + c_{55}q_x^2 + c_{33}\gamma^2 - \rho\omega^2) & ((e_{13}+e_{35})q_x\gamma + e_{15}q_x^2 + e_{33}\gamma^2) \\ (e_{11}q_x^2 + (e_{31}+e_{15})q_x\gamma + e_{35}\gamma^2) & ((e_{14}+e_{36})q_x\gamma + e_{16}q_x^2 + e_{34}\gamma^2) & ((e_{13}+e_{35})q_x\gamma + e_{15}q_x^2 + e_{33}\gamma^2) & \epsilon(-q_x^2 - \gamma^2) \end{bmatrix} \times \begin{bmatrix} u_x \\ u_y \\ u_z \\ \Phi \end{bmatrix} = \mathbf{0}, \tag{12}$$

where all c, e elements are functions of rotational angles, so the elements given here are not necessarily the same as those given for $\mathbf{c}_0, \mathbf{e}_0$, but refer to the rotated parameter matrices $\mathbf{c}, \mathbf{e}$. The above matrix can be employed to visualize element couplings, as,

e.g., in the case of no rotation, where

$$\begin{bmatrix} c_{44}\gamma^2 - \rho\omega^2 + c_{11}q_x^2 & 0 & \gamma q_x(c_{12}+c_{44}) & 0 \\ 0 & c_{44}\gamma^2 - \rho\omega^2 + c_{44}q_x^2 & 0 & 2e_{14}\gamma q_x \\ \gamma q_x(c_{12}+c_{44}) & 0 & c_{11}\gamma^2 - \rho\omega^2 + c_{44}q_x^2 & 0 \\ 0 & 2e_{14}\gamma q_x & 0 & -\epsilon\left(\gamma^2+q_x^2\right) \end{bmatrix} \begin{bmatrix} u_x \\ u_y \\ u_z \\ \Phi \end{bmatrix} = \mathbf{0}, \tag{13}$$

making it clearly visible that $u_x - u_z$ and $u_y - \Phi$ are coupled, respectively, but there is no coupling between u_x,u_z and Φ. This is a direct consequence of Eqs. (3) and (4), but will vary in terms of crystal orientation. Note that in this specific case, the values of the parameter components equal the ones from $\mathbf{c}_0$,$\mathbf{e}_0$ as all rotational angles are zero.

This is particularly interesting, as in this case there is no clear distinction between acoustic and optical phonons anymore, as already mentioned in Ref. [26], and acousto-optical phonons can be excited by light.

The allowed z wave numbers γ are found by solving the secular equation corresponding to Eq. (12). This yields an eight-degree polynomial in γ—hence there are generally eight linearly independent solutions for the system. We write them as

$$u_x = \sum_{j=1}^{8} A_{x,j} \exp(i\gamma_j z), \tag{14}$$

$$u_y = \sum_{j=1}^{8} A_{y,j} \exp(i\gamma_j z), \tag{15}$$

$$u_z = \sum_{j=1}^{8} A_{z,j} \exp(i\gamma_j z), \tag{16}$$

$$\phi = \sum_{j=1}^{8} A_{\phi,j} \exp(i\gamma_j z). \tag{17}$$

For high-symmetry directions such as the ones shown in Fig. 1, with the z axis being aligned to cube edges or diagonals, the eight-degree polynomial will in fact become a fourth-degree polynomial in γ^2, causing the solutions for allowed γ to be symmetric around $\gamma = 0$, i.e., $\gamma = \pm\sqrt{\gamma^2}$. In this case one could also write the solutions in terms of cos , sin and distinguish between solutions where u_x is an even function of z (dilational modes) and where u_x is an odd function of z (flexural modes). For most general orientations, however, the distinction between dilational and flexural modes is not possible [31]. The slab boundary conditions are $T_{xz} = 0, T_{yz} = 0$, and $T_{zz} = 0$ at $z = \pm a/2$. For convenience, only one example, $T_{zz} = 0$ at $z = a/2$, is given here. It reads

$$\begin{aligned} & i\sum_{j=1}^{8}\left(c_{13}q_x + c_{35}\gamma_j\right)A_{xj}\exp\left(i\gamma_j\frac{a}{2}\right) \\ & + i\sum_{j=1}^{8}\left(c_{36}q_x + c_{34}\gamma_j\right)A_{yj}\exp\left(i\gamma_j\frac{a}{2}\right) \\ & + i\sum_{j=1}^{8}\left(c_{35}q_x + c_{33}\gamma_j\right)A_{zj}\exp\left(i\gamma_j\frac{a}{2}\right) \\ & + i\sum_{j=1}^{8}\left(e_{13}q_x + e_{33}\gamma_j\right)A_{\phi j}\exp\left(i\gamma_j\frac{a}{2}\right) = 0, \end{aligned} \tag{18}$$

with the other polarizations and $z = -a/2$ being of similar form.

The electrical conditions are continuity of E_x and D_z at $z = \pm a/2$. For the regions outside the slab, the charge-free Poisson equations yield

$$-q_x^2\Phi + \frac{\partial^2\Phi}{\partial z^2} = 0, \tag{19}$$

with solutions

$$\Phi = [\Phi_+ \exp(-q_x z) + \Phi_- \exp(q_x z)] \exp(iq_x x). \tag{20}$$

Boundedness of solutions leads to

$$\Phi(z) = \phi_- \exp(q_x z)\exp(iq_x x) \text{ for } z < -a/2, \tag{21}$$

$$\Phi(z) = \phi_+ \exp(-q_x z)\exp(iq_x x) \text{ for } z > a/2. \tag{22}$$

Hence, the conditions for $E_x = -\partial\Phi/\partial x$ at both boundaries read

$$iq_x\sum_{j=1}^{8} A_{\phi j}\exp\left(i\gamma_j\frac{a}{2}\right) = iq_x\phi_+\exp\left(-q_x\frac{a}{2}\right), \tag{23}$$

$$iq_x\sum_{j=1}^{8} A_{\phi j}\exp\left(-i\gamma_j\frac{a}{2}\right) = iq_x\phi_-\exp\left(-q_x\frac{a}{2}\right). \tag{24}$$

The corresponding conditions for D_z are (only the one for $a/2$ shown here)

$$\begin{aligned} & -\epsilon i\sum_{j=1}^{8}\gamma_j A_{\phi j}\exp\left(i\gamma_j\frac{a}{2}\right) \\ & + i\sum_{j=1}^{8}(e_{31}q_x + e_{35}\gamma_j)A_{xj}\exp\left(i\gamma_j\frac{a}{2}\right) \\ & + i\sum_{j=1}^{8}(e_{36}q_x + e_{34}\gamma_j)A_{yj}\exp\left(i\gamma_j\frac{a}{2}\right) \\ & + i\sum_{j=1}^{8}(e_{35}q_x + e_{33}\gamma_j)A_{zj}\exp\left(i\gamma_j\frac{a}{2}\right) \\ & - \epsilon_0 q_x\phi_+\exp\left(-q_x\frac{a}{2}\right) = 0. \end{aligned} \tag{25}$$

In total there are 34 unknown coefficients that can be determined by the differential equations and boundary conditions given above: for each γ_i we use three rows of the matrix in Eq. (12) (which has a rank of 3 for each γ_i) and finally add the ten boundary condition equations. Phonon modes are then found by finding pairs of q_x,ω causing the 34×34 system matrix to become singular.

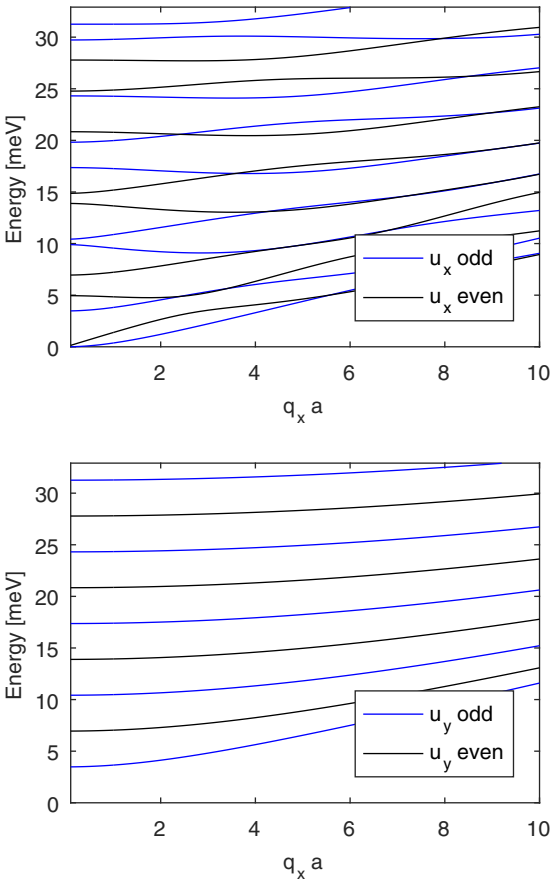

FIG. 2. Dispersion for case I (upper, xz polarization; lower, $y\Phi$ polarization).

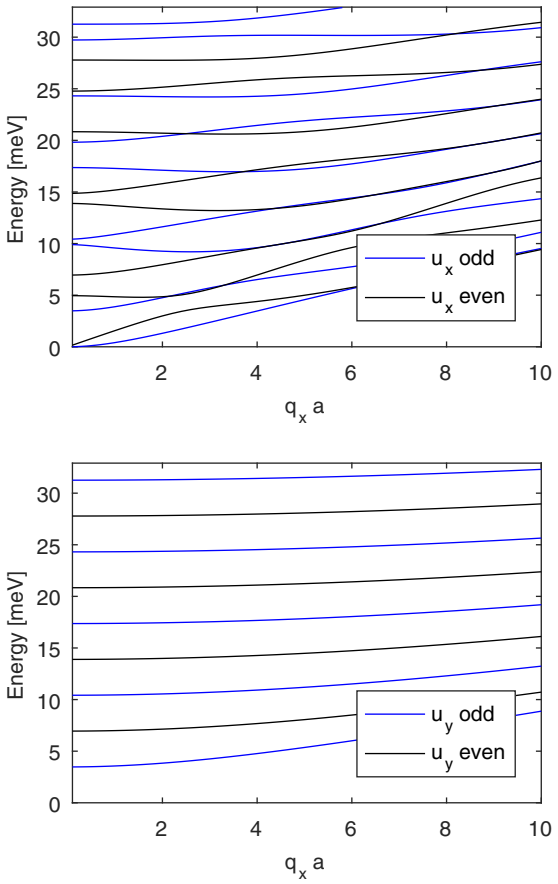

FIG. 3. Dispersion for case II (upper, $xz\Phi$ polarization; lower, y polarization).

III. RESULTS

We solved the system described above for several symmetric orientations for the five cases: I–V shown in Figs. 1(a)–1(e), respectively. Note that case I has in principle already been treated in Ref. [26], but is included here for the sake of completeness (we stress that Figs. 1 and 2 in Ref. [26] show dispersion curves for the so-called type I modes and only modes from a certain minimum energy above zero starting from $q_x a = 0$ are plotted). The results are obtained for a slab of GaAs and width $a = 2$ nm. In these cases, all results can be split up into dilational and flexural modes.

A. Case I: $\theta = 0, \phi = 0, \psi = 0$

The modes here are seen to have the polarizations $u_x - u_z$ decoupled from $u_y - \Phi$. This problem has been studied before, although often under the assumption of isotropy, which clearly is not the case. The dispersion curves are shown in Fig. 2.

B. Case II: $\theta = 0, \phi = \pi/4, \psi = 0$

For this case, the coupling pattern changes: The u_y solution is decoupled from the others, while the u_x,u_z, and Φ solutions are fully coupled. The dispersion curves are shown in Fig. 3.

C. Case III: $\theta = 0, \phi = 0, \psi = \pi/4$

In this case, the coupling changes again and is in fact similar to case I. The dispersion curves are shown in Fig. 4. In fact, it is noticeable that the lowest-energy $u_x - u_z$ dispersion curves are somewhat similar to case I as well, with the higher energies differing in the sense that, for greater q_x values, even and odd modes have very similar energies.

D. Case IV: $\theta = \pi/4, \phi = 0, \psi = 0$

In this case, again the y-polarized modes are uncoupled from the other modes, similar to case II. The dispersion curves are shown in Fig. 5. One of the more interesting observations is that the mode density for the y-polarized modes is much greater (almost double) than in the cases where y is coupled with Φ and also visibly larger than for the y polarization in case II (Fig. 3).

E. Case V: $\theta = \pi/4, \phi = \cos^{-1}(1/\sqrt{3}), \psi = 0$

In this case, there is no decoupled polarization—all x, y, z, ϕ polarizations are directly coupled and hence only acousto-optical phonon modes can exist when the coordinate axes are oriented along the body diagonals of the unit cell. The dispersion curves are shown in Fig. 6.

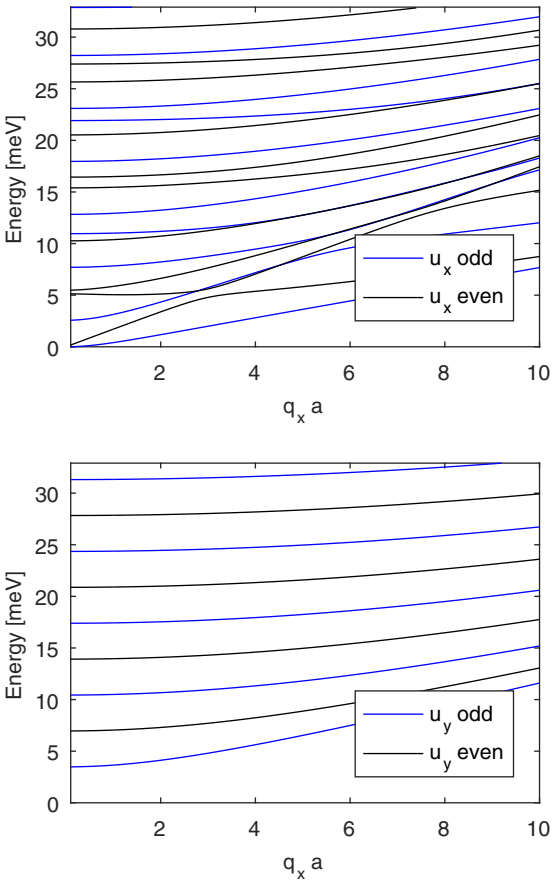

FIG. 4. Dispersion for case III (upper, xz polarization; lower, $y\Phi$ polarization).

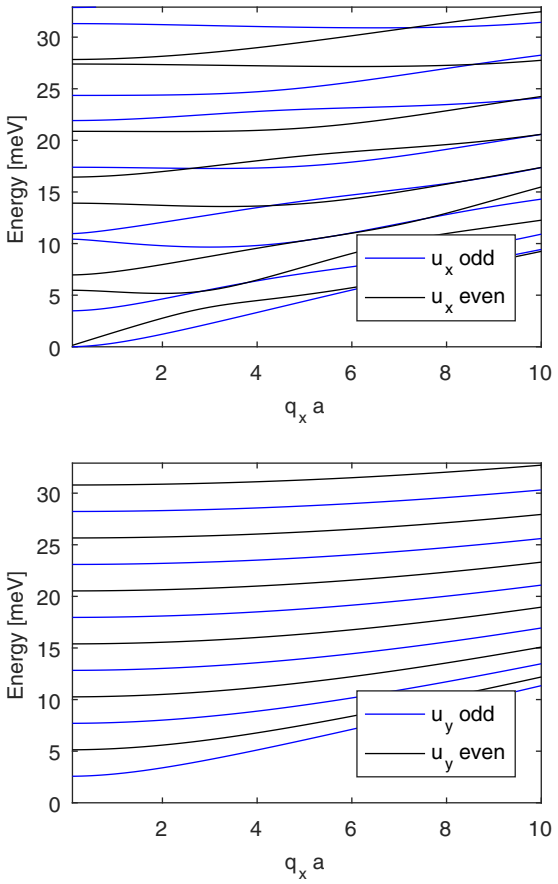

FIG. 5. Dispersion for case IV (upper, $xz\Phi$ polarization; lower, y polarization).

F. Application of spatially limited electric potential

For visualizing the effect of change in crystal-growth direction on a more practical setup, we have used the formalism above to solve for the electromechanical fields in the infinite slab excited by a voltage applied across a portion of the slab ends. This is done by expanding a top hat function in x of potential V_0 into a Fourier space and subsequently solving the same equations as before, with the exception that the boundary conditions for the potential have changed ($V = V_0$ at $z = 1, -20 \leqslant x \leqslant 20$ nm, else $V = 0$ on all other boundaries). Still, the overall dependency on crystal orientation remains intact. Mathematically, the solutions are written as summations of Eqs. (14)–(17) over q_x:

$$u_x(x,z,t) = \sum_{n=1}^{n_{\max}} \sum_{j=1}^{8} A_{xnj} \exp(i\gamma_{nj} z) \exp(i q_{xn} x), \quad (26)$$

$$u_y(x,z,t) = \sum_{n=1}^{n_{\max}} \sum_{j=1}^{8} A_{ynj} \exp(i\gamma_{nj} z) \exp(i q_{xn} x), \quad (27)$$

$$u_z(x,z,t) = \sum_{n=1}^{n_{\max}} \sum_{j=1}^{8} A_{znj} \exp(i\gamma_{nj} z) \exp(i q_{xn} x), \quad (28)$$

$$\phi(x,z,t) = \sum_{n=1}^{n_{\max}} \sum_{j=1}^{8} A_{\phi nj} \exp(i\gamma_{nj} z) \exp(i q_{xn} x), \quad (29)$$

where q_{xn} is the discretized version of q_x with $n_{\max}$ evenly distributed sampling points—hence this is a discrete Fourier transform. In our case, q_x was discretized in the interval -10^{10} to 10^{10} with a step size of approximately 1×10^5, corresponding to $n_{\max} = 128\,000$ steps and convergence in $n_{\max}$ was checked for. Due to its periodic nature, the transform will cause periodic solutions with a period of about 10^{-5}m. To evade interference issues, we have slightly perturbed the material stiffness by adding a damping term: $\mathbf{c} \rightarrow \mathbf{c} \cdot (\mathbf{I} + 0.0001 \cdot i \cdot \mathbf{I})$. This does not cause noticeable deviations close

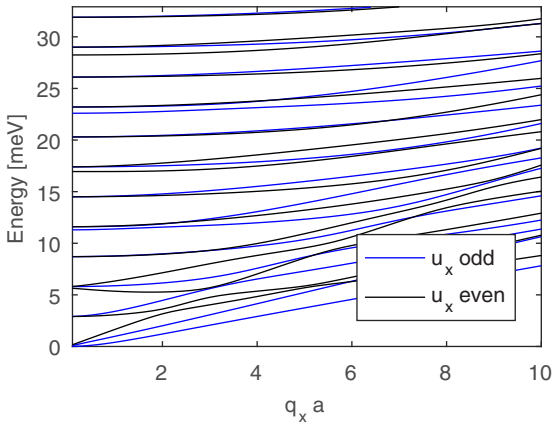

FIG. 6. Dispersion for case V. All polarizations are coupled.

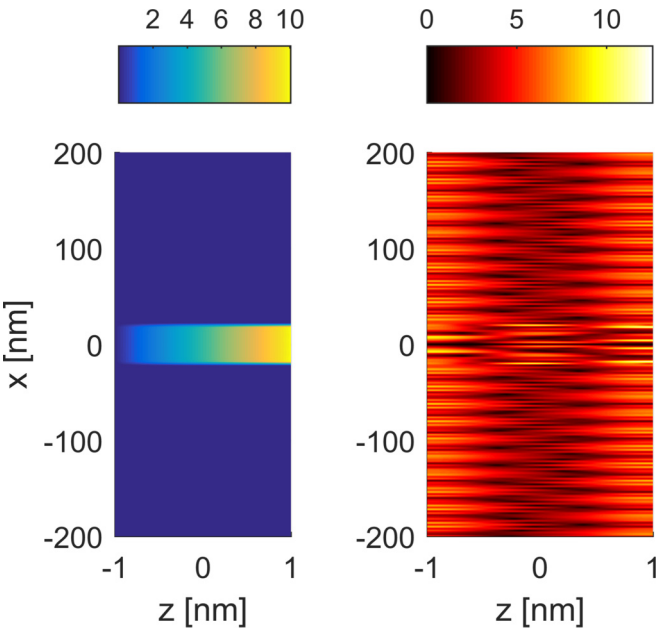

FIG. 7. Applied potential to case I. Electric potential ϕ (V, left) and corresponding $|u_y|$ (pm, right) for $f = 2 \times 10^{12}$ Hz (corresponding to 8.2 meV).

to the sources, but damps out the outgoing wave before generating any interferences with the period counterparts.

The result for the [001] growth direction (case I) is shown in Fig. 7 for $V_0 = 10$ V applied to a short central area with a 40-nm width along the x axis of the slab. In the figure it is clearly seen that the application of the electric potential over a limited space excites a corresponding acousto-optical wave that can be seen propagating towards $\pm\infty$ in the x direction.

We have done the same analysis for the [111] growth direction (case V), shown in Fig. 8, again for $V_0 = 10$ V. Here, a different wave propagation pattern is observed. It is now possible to see both high-q_x and low-q_x components in the wave pattern as opposed to the [001] growth direction that has q_x components about three times higher than the lowest in the [111] case. Also the high-q_x components primarily stem from the lower-energy bands shown in the dispersion curves. This demonstrates a major change in electromechanical coupling depending on the growth direction of the freestanding quantum well. The mechanical amplitudes of the deformation are approximately equal for the two growth directions and correspond to a strain of about 0.1%. For the u_z deformation it also becomes very clear how the change in crystal-growth direction influences the different polarizations in very distinct manners. Here, the major deformation is located very close to the source, while one can even observe a small "shear boundary" at $x = -20$ and 20 nm for the u_x case—but else the energy is distributed much more evenly in the slab domain compared to the u_z case.

G. Plasma influence on phonons

To emphasize the importance of the previous results, we will now turn our attention towards a nonobvious consequence. As we have demonstrated, the coupling of phonon modes strongly depends on the unit crystal orientation. Furthermore, Eq. (12)

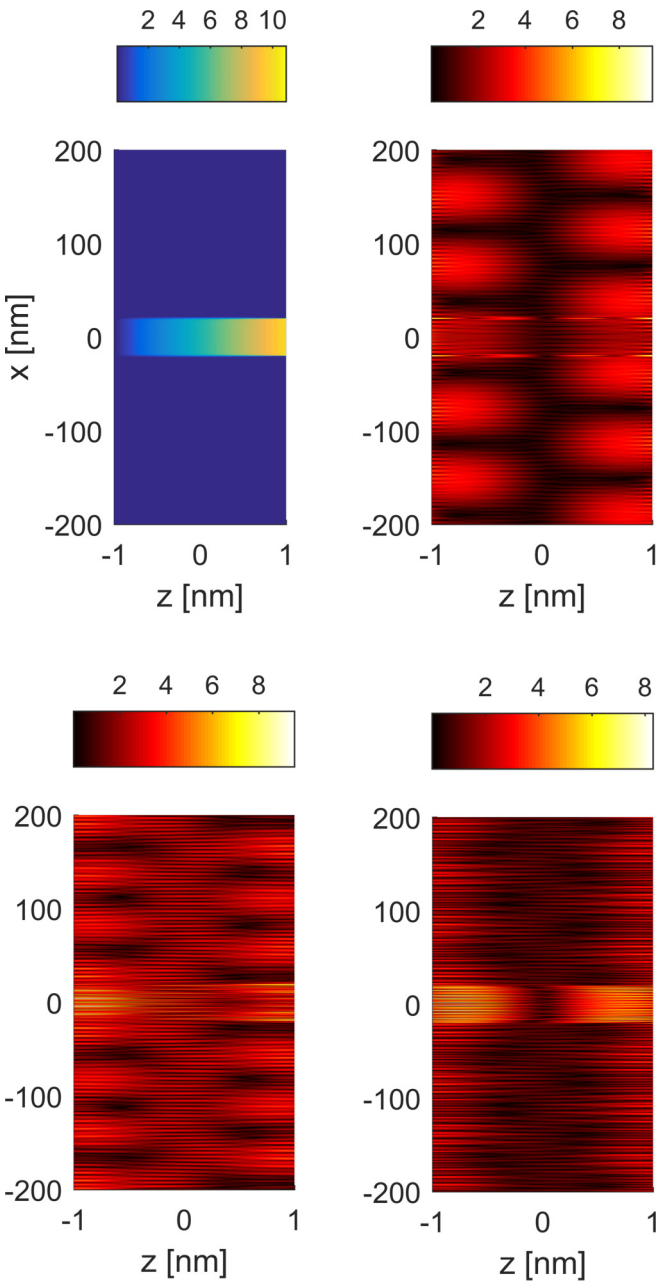

FIG. 8. Applied potential to case V. Electric potential ϕ (V, upper left) and corresponding $|u_x|$ (pm, upper right), $|u_y|$ (pm, lower left), and $|u_z|$ (pm, lower right) for $f = 2 \times 10^{12}$ Hz (corresponding to 8.2 meV).

shows that the phonon modes generally are influenced by the dielectric constant. In particular, the dielectric constant is not a constant function of frequency but approaches zero near the plasma frequency. Hence, the effective, or piezoelectric stiffened, mechanical stiffness changes drastically near the plasma frequency, thereby significantly changing the strength of the acousto-optical phonon coupling. To emphasize this effect, we will use the Drude model for the permittivity given by [32,33]

$$\epsilon(\omega) = \epsilon_\infty \left(1 - \frac{\omega_p^2}{\omega^2 + \tau^{-2}}\right), \tag{30}$$

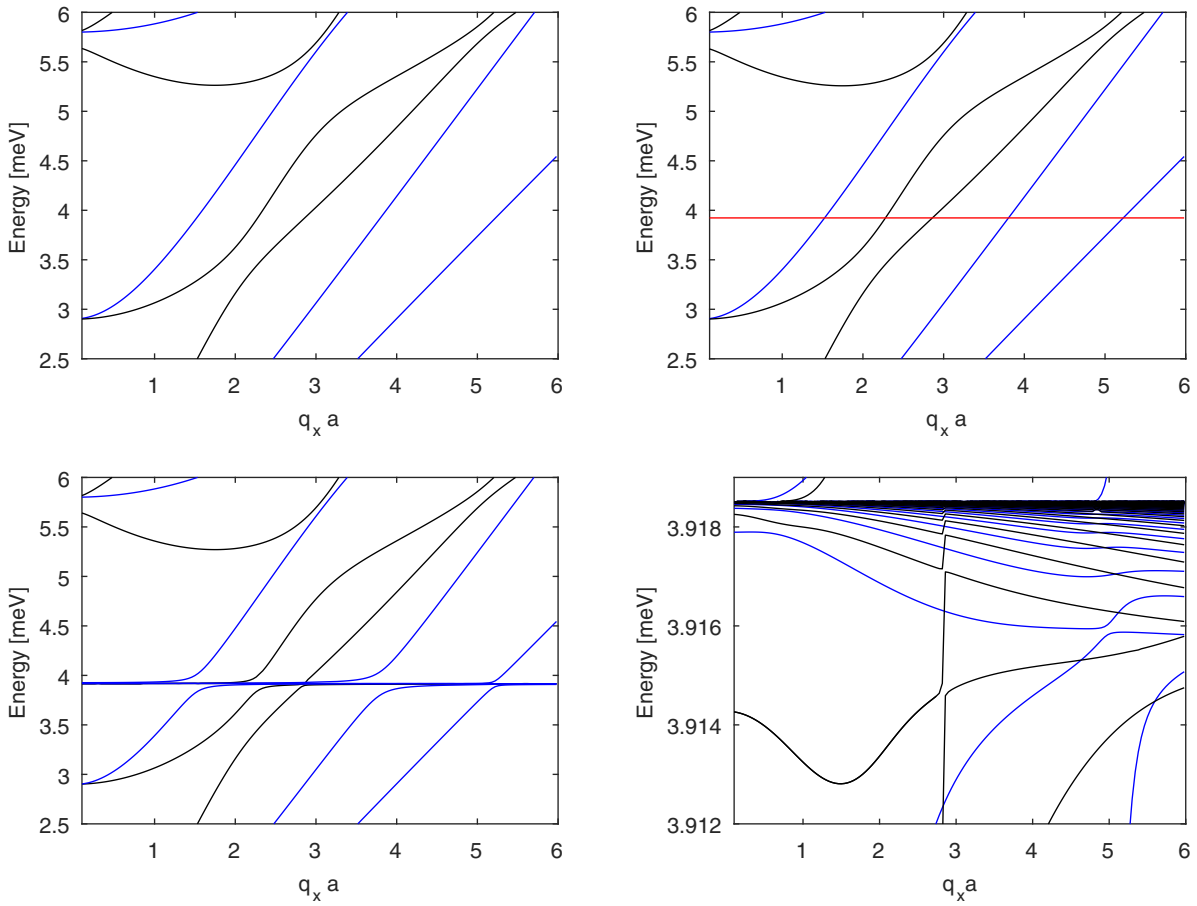

FIG. 9. Dispersion for case V (from top left to bottom right: $\epsilon = \epsilon_\infty, e \neq 0$; $\epsilon = \epsilon(\omega), e = 0$; $\epsilon = \epsilon(\omega), e \neq 0$; zoom-in on the energy band for $\epsilon = \epsilon(\omega), e \neq 0$). The blue curves indicate u_x odd modes while black curves indicate u_x even modes. The red curve in the second plot corresponds to the confined optical mode for $\epsilon(\omega) = 0$.

where τ and ω_p are the carrier scattering time and plasma frequency, respectively and lossless conditions are assumed. These two parameters are given by

$$\tau = \frac{m_{\text{eff}} \cdot \mu_{DC}}{q}, \tag{31}$$

$$\omega_p = \sqrt{\frac{Nq^2}{m_{\text{eff}}\epsilon_\infty}}, \tag{32}$$

where μ_{DC} is the carrier mobility, N is the carrier density, q is the fundamental charge, and m_{eff} is the electron effective mass. Notice that the plasma frequency can be tuned by doping (which in principle also applies to the scattering time, but we neglect that dependence here for simplicity). In our example, we choose a carrier density of 1.25×10^{16} cm^{-3}, e.g., realized by introducing a moderate concentration of dopants to intrinsic GaAs, resulting in a plasma frequency of $\hbar\omega_p = 4.41$ meV while $\tau = 0.32$ ps.

For demonstration purposes, we will consider case V in the case $q_x = 0$ where analytical results can be obtained. The dispersion relation simplifies to

$$\omega_n^2 = \left(c_{33} + \frac{e_{33}^2}{\epsilon_\infty\left(1 - \frac{\omega_p^2}{\omega_n^2 + \tau^{-2}}\right)} \right) \frac{n^2\pi^2}{\rho a^2}. \tag{33}$$

It is seen that the piezoelectric stiffened dispersion relation is of second order in ω_n^2. It is also evident that in the limit of $n \to \infty$, one of the two ω_n converges towards the usual

$$\omega_n = \sqrt{\frac{1}{\rho}\left(c_{33} + \frac{e_{33}^2}{\epsilon_\infty}\right)}\frac{n\pi}{a}, \tag{34}$$

while the other (for all n values) converges to the solution of

$$\left(c_{33} + \frac{e_{33}^2}{\epsilon_\infty}\right)(\omega_n^2 + \tau^{-2}) = w_p^2 c_{33}. \tag{35}$$

In our case the latter yields a phonon energy of 3.9 meV. Therefore we can expect an energy band where the local phonon density is much higher and in the mathematical limit $n \to \infty$ approaches infinity. For the cases where q_x is nonzero, the solution is not readily obtained but it can be found using the same framework described previously. The new dispersion curves are shown in Fig. 9 for the cases in which (a) ϵ is constant and $e \neq 0$, (b) $\epsilon(\omega)$ is based on the Drude mode with $e = 0$, and (c) $\epsilon(\omega)$ and $e \neq 0$, respectively. The figure shows the expected appearance of a phonon band around 3.9 meV and the effect it has on the classical dispersion curves. When a constant ϵ is assumed this band does not occur. When the piezocoupling is disabled ($e = 0$), the band consists of a single mode given by $\epsilon(\omega) = 0$. In the absence of the

piezoelectric effect, this mode does not interact with the other modes, i.e., the latter practically coincide with the constant epsilon modes. In the case where the Drude model is used and the piezoelectric effect is effective, an energy band of high phonon mode density is generated around 3.9 meV. This band separates in energy the modes obtained in the constant ϵ case, into regions above and below the band, since all modes are piezoelectrically coupled. For cases I-IV where some modes are not coupled by the piezoelectric effect a distinct energy separation of modes is not effective. A closer inspection of the band, shown in the last graph in Fig. 9, reveals that the phonon density of modes increases drastically in the band region. Our calculations show a density of up to 10^5 meV^{-1} (for constant q_x), which is the limit of our numerical grid for finding modes.

With this in mind it is possible to tune phonon energies by changing the plasma frequency, e.g., through a carrier density change. We note in passing that the plasma frequency of GaAs is low due to the low intrinsic charge-carrier density (2.1×10^6 cm^{-3}). It is also seen that the piezoelectric effect itself is of important interest in regions close to this energy band as the difference between the classical model with and without the piezoelectric effect is small except when ϵ becomes small.

IV. DISCUSSION

As we can see from the dispersion curves, there are no high-symmetry directions where the electrical potential is not coupled to acoustic vibrations, hence for all high-symmetry directions acousto-optical phonons exist. Due to the different nature in couplings ($xz\Phi$, $y\Phi$, $xyz\Phi$), the density of acousto-optical modes changes significantly depending on crystal orientation. A consequence is that, for the cases II, IV, and V, the lowest allowed acousto-optical phonon energies are significantly lower than for cases I and III (about a factor of 4 for $q_x a = 1$). This is due to the fact that for cases II, IV, and V the electrical potential is linked to the xz modes instead of the y modes (and all modes in case V). The density of acousto-optical phonon states in case V is largest, due to the full coupling of all states; it is approximately two to three times greater than in the other cases, with the $y - \phi$ polarization showing the lowest densities in general.

Further, we have shown the significance of crystal-growth direction for the generated acousto-optical phonon field due to orientation-dependent mode excitation. This result, directly linked to the increase in opto-acousto-optical phonon density, may have important implications for quantum processing applications.

Finally, we have investigated the effect that a nonconstant dielectric constant has on the phonon dispersion due to the piezoelectric coupling. We have found that an additional energy band is generated where the classical, i.e., non-piezo-coupled, phonon dispersion curves split into two components due to the piezoelectric effect (but still there is no overlap between same-symmetry dispersion curves): one above the band and one below. The latter could potentially be exploited in tuning phonon properties in semiconductor based devices.

V. CONCLUSION

In conclusion, we have investigated two different types of phonons (acoustic and acousto-optical) coupled by the piezoelectric effect. We have shown a significant dependence of the phonon dispersion in a piezoelectric slab (GaAs) on the crystal orientation, as opposed to previously employed isotropic assumptions. Not only do the dispersion curves change shape, but the density of modes differs significantly, stipulating significant changes in, e.g., the magnitudes of electron-phonon scattering mechanisms, specifically because the density of acousto-optical phonons depends strongly on crystal orientation (even small deviations from high-symmetry orientations can cause a doubling of mode density of acousto-optical phonons). Furthermore, it implies local defects in a high-symmetry lattice can cause local increase in phonon density and thereby local increase of electron-phonon scattering. This strong crystal orientation dependence could have a significant impact in terms of photon absorption spectra. We finally demonstrate that piezoelectricity substantially increases the strength of the acousto-optical phonon coupling, and thus the phonon density of states, near the plasma frequency.

[1] R. Valin, M. Aldegunde, A. Martinez, and J. R. Barker, J. Appl. Phys. **116**, 084507 (2014).

[2] C. Hopfmann, A. Musiał, M. Strauß, A. M. Barth, M. Glässl, A. Vagov, M. Strauß, C. Schneider, S. Höfling, M. Kamp, V. M. Axt, and S. Reitzenstein, Phys. Rev. B **92**, 245403 (2015).

[3] J. H. Quilter, A. J. Brash, F. Liu, M. Glässl, A. M. Barth, V. M. Axt, A. J. Ramsay, M. S. Skolnick, and A. M. Fox, Phys. Rev. Lett. **114**, 137401 (2015).

[4] S. Bounouar, M. Müller, A. M. Barth, M. Glässl, V. M. Axt, and P. Michler, Phys. Rev. B **91**, 161302 (2015).

[5] M. Glässl, A. M. Barth, and V. M. Axt, Phys. Rev. Lett. **110**, 147401 (2013).

[6] T. M. Stace, A. C. Doherty, and S. D. Barrett, Phys. Rev. Lett. **95**, 106801 (2005).

[7] M. J. Gullans, Y.-Y. Liu, J. Stehlik, J. R. Petta, and J. M. Taylor, Phys. Rev. Lett. **114**, 196802 (2015).

[8] A. Auffèves, J.-M. Gérard, and J.-P. Poizat, Phys. Rev. A **79**, 053838 (2009).

[9] T. Yoshie, A. Scherer, J. Hendrickson, K. Khitrova, H. Gibbs, G. Rupper, C. Ell, O. Shchekin, and D. G. Deppe, Nature (London) **432**, 200 (2004).

[10] K. Roy-Choudhury and S. Hughes, Phys. Rev. B **92**, 205406 (2015).

[11] E. Knill, R. Laflamme, and G. Milburn, Nature (London) **409**, 46 (2001).

[12] P. Kaer, T. R. Nielsen, P. Lodahl, A.-P. Jauho, and J. Mørk, Phys. Rev. Lett. **104**, 157401 (2010).

[13] Z. Wang, Adv. Mater. **19**, 889 (2007).

[14] W. Wu, L. Wang, Y. Li, F. Zhang, L. Lin, S. Niu, D. Chenet, X. Zhang, Y. Hao, T. F. Heinz, J. Hone, and Z. L. Wang, Nature (London) **514**, 470 (2014).
[15] K. Kaasbjerg, K. S. Thygesen, and A.-P. Jauho, Phys. Rev. B **87**, 235312 (2013).
[16] R. P. G. McNeil, M. Kataoka, C. J. B. Ford, C. H. W. Barnes, D. Anderson, G. A. C. Jones, I. Farrer, and D. A. Ritchie, Nature (London) **477**, 439 (2011).
[17] M. V. Gustafsson, P. V. Santos, G. Johansson, and P. Delsing, Nat. Phys. **8**, 338 (2012).
[18] J. Schiefele, J. Pedrós, F. Sols, F. Calle, and F. Guinea, Phys. Rev. Lett. **111**, 237405 (2013).
[19] M. Farhat, S. Guenneau, and H. Bağcı, Phys. Rev. Lett. **111**, 237404 (2013).
[20] E. A. Muljarov, T. Takagahara, and R. Zimmermann, Phys. Rev. Lett. **95**, 177405 (2005).
[21] P. Borri, W. Langbein, U. Woggon, V. Stavarache, D. Reuter, and A. D. Wieck, Phys. Rev. B **71**, 115328 (2005).
[22] C.-Y. Hsieh, Y.-P. Shim, M. Korkusinski, and P. Hawrylak, Rep. Prog. Phys. **75**, 114501 (2012).
[23] N. Bannov, V. Aristov, V. Mitin, and M. A. Stroscio, Phys. Rev. B **51**, 9930 (1995).
[24] J. J. Licari and R. Evrard, Phys. Rev. B **15**, 2254 (1977).
[25] K. L. Kliewer and R. Fuchs, Phys. Rev. **144**, 495 (1966).
[26] M. Willatzen and Z. L. Wang, Phys. Rev. B **92**, 224101 (2015).
[27] P. Waltereit, O. Brandt, A. Trampert, H. T. Grahn, J. Menniger, M. Ramsteiner, M. Reiche, and K. H. Ploog, Nature (London) **406**, 865 (2000).
[28] L. Duggen, M. Willatzen, and B. Lassen, Phys. Rev. B **78**, 205323 (2008).
[29] C. Kittel, *Introduction to Solid State Physics*, 8th ed. (Wiley, Hoboken, NJ, 2005).
[30] B. Auld, *Acoustic Fields and Waves in Solids*, 2nd ed. (Krieger, Malabar, FL, 1990), Vol. 1.
[31] B. Auld, *Acoustic Fields and Waves in Solids*, 2nd ed. (Krieger, Malabar, FL, 1990), Vol. 2.
[32] B. Tata and A. Arora, Infrared Phys. **24**, 547 (1984).
[33] M. Willatzen and J. Christensen, Phys. Rev. B **89**, 041201 (2014).